Supporting Information for "Wintertime Brine Discharge at the Surface of a Cold Polar Glacier and the Unexpected Absence of Associated Seismicity"

C. G. Carr[1,2], J. D. Carmichael[2], E. C. Pettit[3]

[1]University of Alaska Fairbanks, Fairbanks, AK, USA

[2]Los Alamos National Laboratory, Los Alamos, NM, USA

[3]Oregon State University, Corvallis, OR, USA

Contents of this file

Additional Supporting Information (Files uploaded separately)

1. Captions for Movies S1 to S2

Introduction

This supporting information includes 11 additional figures, 1 table, 2 movies, and their supporting text.

Corresponding author: Chris G. Carr, Los Alamos National Laboratory, Los Alamos, NM 87544, USA (cgcarr@lanl.gov)

Upon review of data collected by the time-lapse camera, we realized that the time zone corresponding to the internal camera clock had not been recorded. Field photos taken on personal cameras during the time-lapse camera installation as well as metadata from a co-located seismometer guided our time zone correction of the time-lapse images from the camera. The camera time appears to correspond to UTC-13 at the time of installation, and the camera clock observes daylight savings time following the dates for the United States. We therefore add 12 hours for timestamps between 9 March and 2 November 2014, and add 13 hours during the rest of the year. We estimate that our corrected times of day are within about 1–2 hours of the true time of day based on sunlight patterns. Despite the lack of temporal accuracy, we can still make observations about the relative timing of brine release pulses as well as erosional and depositional characteristics; however, we cannot tie any specific photo to discrete seismic events. We note that even with accurate timestamps, the relatively coarse time resolution of the photos (1 sample every 2 hours) would hinder direct correlation with specific events in the seismic record (200 samples per second).

Text S1. Description of Additional Figures

A large crack in the glacier surface was visible following the winter 2014 brine release (Figure S1). This photo from 21 November 2014 shows the brine icing largely intact, with some incised meltwater channels. The lake ice and moat appear to be still frozen.

A meteorological station (Doran & Fountain, 2019) located on Taylor Glacier collected air temperature (Figure S2) and wind speed during the duration of our seismic experiment. A previous study at Taylor Glacier modeled melt occurring at temperatures as low as -2.7°C during the summer season due to solar radiation (Hoffman et al., 2008). However, the brine release events documented in our study occurred when air temperatures were well below this threshold; therefore, we assume negligible surface melt. Air temperatures at the Lake Bonney meteorological station (located on dark rocks and sediment on the south shore of Lake Bonney) follow a similar pattern and are slightly warmer yet still subfreezing. Warm air temperature spikes during winter months correspond with increases in wind speed (Nylen et al., 2004; Speirs et al., 2010).

We generated spectrograms from the seismic data in order to perform a visual data quality check and to qualitatively investigate potential relationships between meteorological variables and spectral features. Spectrograms were generated from the detrended, bandpass-filtered ([2.5, 35] Hz) data using 8 second windows with 5 second overlap. For this initial analysis, we did not remove the instrument response; therefore, the units are related to amplitude in counts rather than ground displacement or velocity.

In Figures S3, S4, and S5, temperature (left y axis) and wind speed (right y axis) are plotted on the upper panel of each subplot; scales vary from month to month to accommodate seasonality. Meteorological data are from the Taylor Glacier station (Doran & Fountain, 2019). The three channels (EHZ: vertical, EHE: east, and EHN: horizontal) are plotted in the lower three panels of each subplot.

We visually inspected spectrograms to identify time periods when data quality was poor, and excluded these days from the Rayleigh wave detection analysis. Examples include data from station CECE prior to servicing in January 2014 (Figure S3a) and station JESS after 9 December 2014 (Figure S5b). During the onset of brine release in May 2014 (Figure S4), we deemed data quality on all channels at all stations to be sufficient for the Rayleigh wave analysis.

Our Rayleigh detector exploited both tails of the statistical distribution as well as correlation between the vertical and transverse channels (with respect to a Blood Falls back azimuth) to detect Rayleigh events arriving from other directions. We plot results from two back azimuths: results from the Blood Falls back azimuth (ZR) are plotted in Figure 3 and results from one non-Blood Falls back azimuth (ZT) are plotted in Figure S6, where ZT is the back azimuth 90°clockwise from the Blood Falls back azimuth for each station (see Figure 2 for back azimuth directions). In other words, these events are arriving from different source directions than Blood Falls. The lighter colors on each time series are the event detection rates for all prescribed CFAR values; the bold lines are the detection rates with a prescribed CFAR of $5x10^{-6}$. The initial Blood Falls brine release is highlighted in red for the CFAR = $5x10^{-6}$ results on all plots.

One limitation of our approach is that we used a restricted set of 4 back azimuth directions for each seismometer rather than scanning through all possible back azimuths. Effectively, we monitor Blood Falls as if it were a point source using the positive tail of the ZR correlogram distribution. However, given the seismometer proximity to Blood Falls, especially in the case of JESS, we would expect that events from the Blood Falls area would arrive from a range of back azimuths. Further, for two otherwise identical Rayleigh events, one located directly along the back azimuth would have higher correlation values than one located at a slightly different back azimuth. Smaller events directly along the back azimuth should thus be more detectable than they otherwise would be if slightly offset from the direct back azimuth. Nonetheless, we can use the event rate time series from a strongly contrasting back azimuth (ZT correlogram) to visualize patterns of non-Blood Falls area Rayleigh-wave seismicity.

In Figures S7 and S8 we plot dominant frequency of identified Rayleigh wave events arriving at each seismic station from a Blood Falls back azimuth against the event duration. Dominant frequency and event duration are calculated as described in the methods section of the main text. In Figure S7, each station's subplot includes all data for all identified Rayleigh events, while in S8 the events are separated by month of year. As in Figure 4, horizontal frequency banding is present. Event duration clusters strongly around 0.6–0.7 seconds, and the distribution of event times is skewed to the left (shorter event duration) with a long right-hand (longer event duration) tail. The clustering of event times suggests a repetitive source with a given physical dimension.

Various cracks in ice are present in the environment near the glacier terminus (Figure S9), including ice blisters (Figure S10). These approximate scale of these cracks ranges from tens of centimeters to several meters in length, with openings on the order of centimeters to tens of centimeters.

In Figure S11, the normalized vertical and horizontal displacement for the Rayleigh eigenfunctions associated with our source model from Appendix B in the main paper are plotted as a function of depth. As described in Appendix B, we used the detector threshold values and sample variance from Table S1 as input values to constrain our source depth model.

Movie S1. Movie created from time-lapse photos, one image per day from 9 May 2014 – 7 June 2014. See introduction section above for an explanation of the time zone correction we applied; all time stamps are given in our best estimate of UTC time. File name: ms01.avi.

Movie S2. Movie created from time-lapse photos, one image per 2 hours except when power loss interrupted data collection. Note the movie retains a placeholder of the most recently availbale image while the counter in the lower left advances, these frames are labelled like “no data, image from 08-Jun-2014 16:47 UTC”. See introduction section above for an explanation of the time zone correction we applied; all time stamps are given in our best estimate of UTC time. File name: ms02.avi.

References

Doran, P. T., & Fountain, A. G. (2019). *McMurdo Dry Valleys LTER: High frequency measurements from Taylor Glacier Meteorological Station (TARM) in Taylor Valley, Antarctica from 1994 to present.* Environmental Data Initiative. doi: 10.6073/pasta/a1df5cdab3319e9adeb18f8448fd363e

Hoffman, M. J., Fountain, A. G., & Liston, G. E. (2008). Surface energy balance and melt thresholds over 11 years at Taylor Glacier, Antarctica. *Journal of Geophysical Research*, *113*(F4), 12 pp. doi: 10.1029/2008JF001029

Nylen, T. H., Fountain, A. G., & Doran, P. T. (2004). Climatology of katabatic winds in the McMurdo Dry Valleys, southern Victoria Land, Antarctica. *Journal of Geophysical Research*, *109*(D03114), 9 pp. doi: 10.1029/2003JD003937

Speirs, J. C., Steinhoff, D. F., McGowan, H. A., Bromwich, D. H., & Monaghan, A. J. (2010). Foehn winds in the McMurdo Dry Valleys, Antarctica: the origin of extreme warming events. *Journal of Climate*, *23*(13), 3577–3598. doi: 10.1175/2010JCLI3382.1

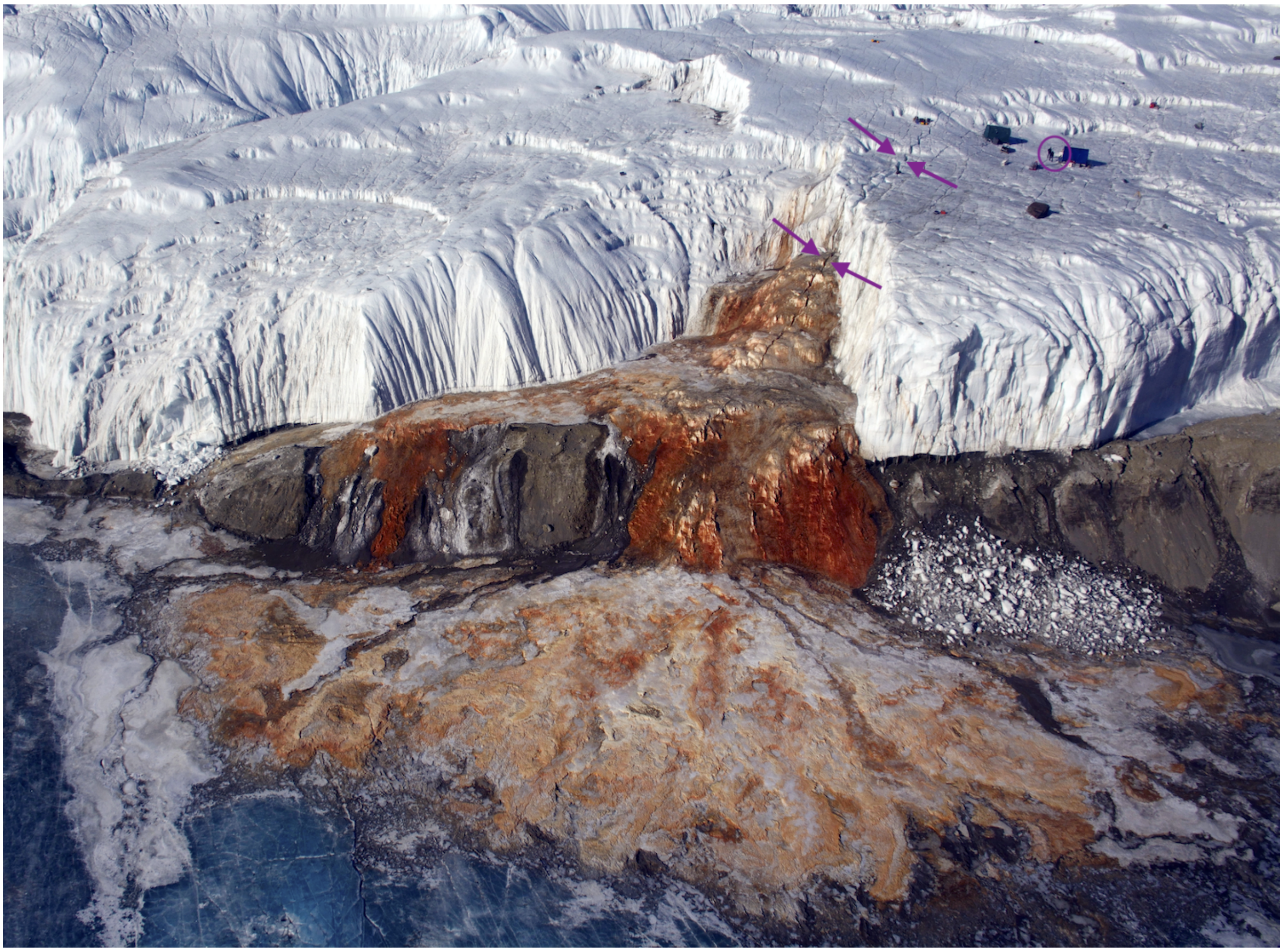

Figure S1. Taylor Glacier terminus following the winter 2014 brine release event. Two sets of purple arrows mark the Blood Falls crevasse; for scale, two people are circled in purple standing next to tents on the glacier surface. Photo: Peter Rejcek, photo date: 21 November 2014. Photo source: National Science Foundation US Antarctic Program Photo Library (https://photolibrary.usap.gov).

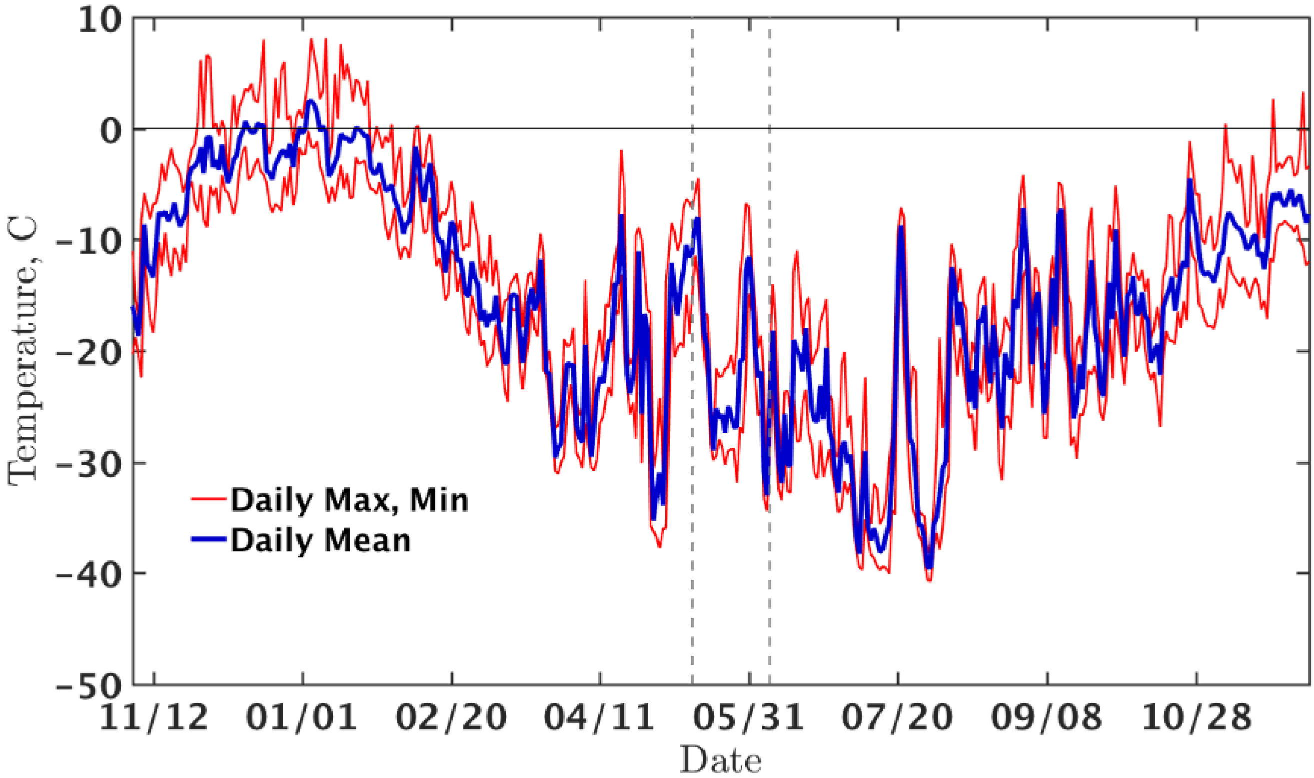

Figure S2. Daily minimum, maximum, and mean air temperatures from November 2013 – November 2014 recorded at the McMurdo Dry Valleys Long Term Ecological Research meteorological station on Taylor Glacier (Doran & Fountain, 2019). Vertical dashed grey lines indicate the onset of observed brine release (12 May – 7 June). Maximum temperature during the highlighted window is −4.1°C (14 May), otherwise temperatures remain below −5.5°C, and average −20.7°C. Horizontal axis labels are day/month.

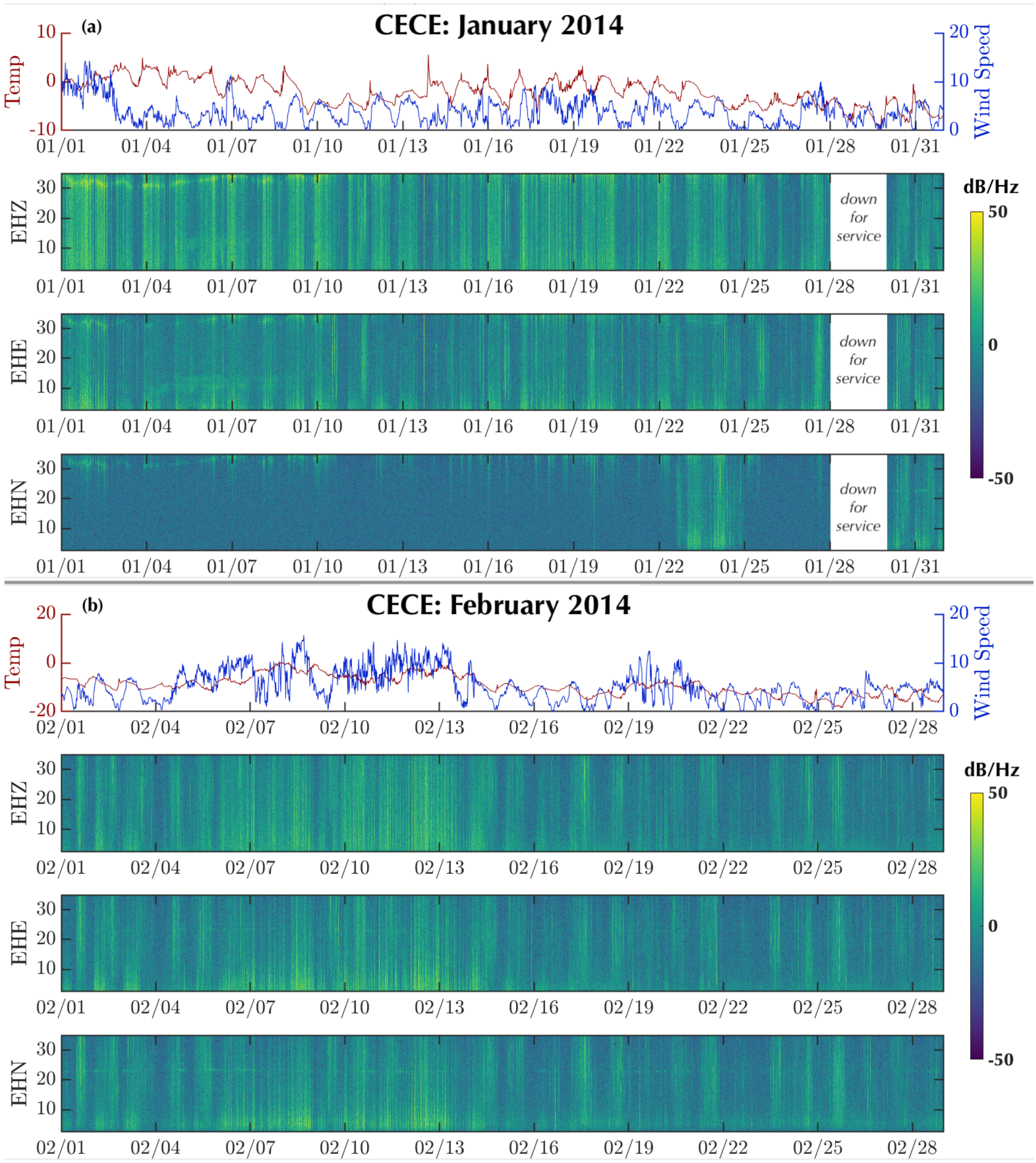

Figure S3. Spectrograms for station CECE for (a) January 2014 and (b) February 2014. Prior to instrument servicing 29 Jan 2014, the north channel (EHN) was not operating properly; the issue was corrected during servicing.

146
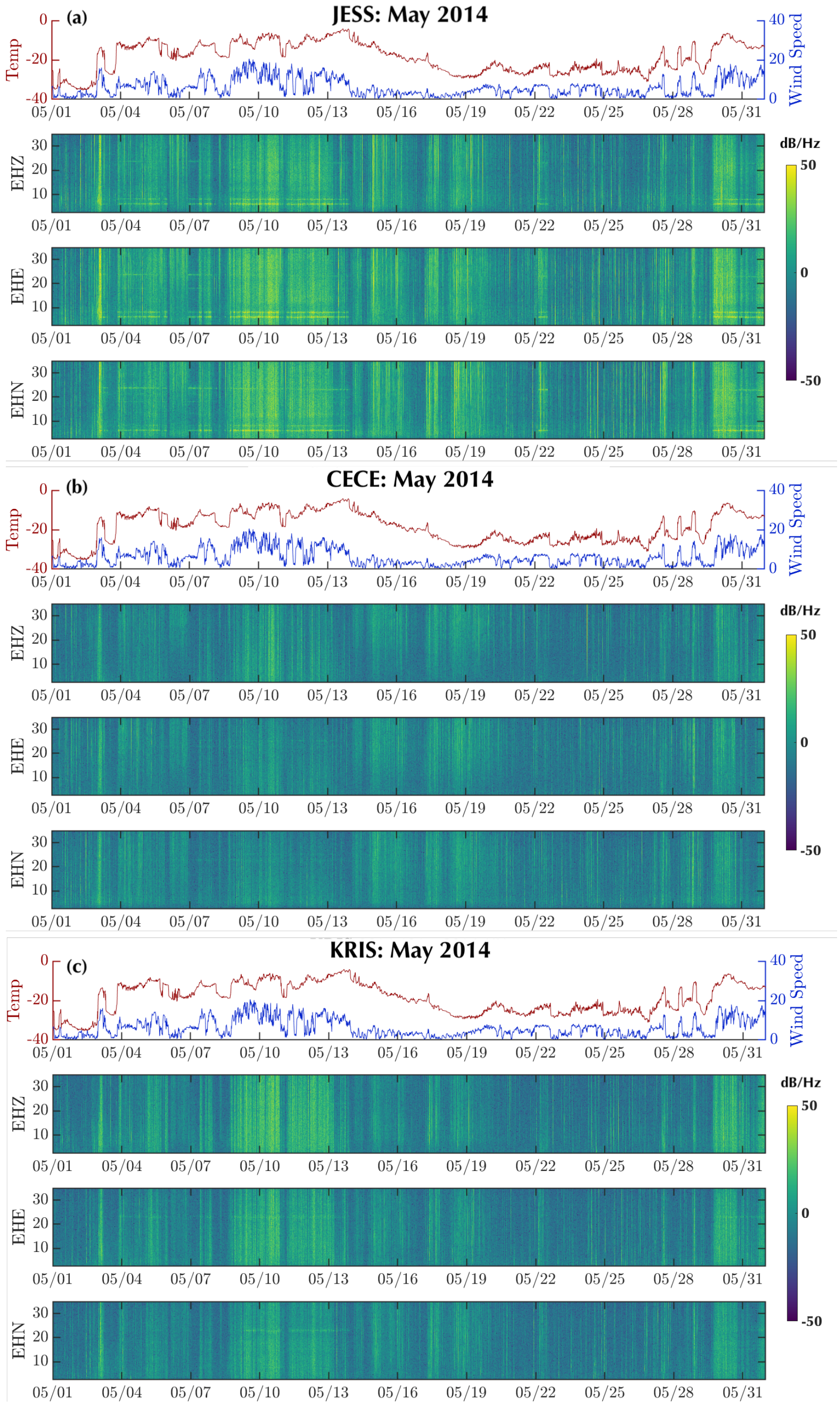

147 **Figure S4.** Spectrograms for all stations for May 2014.

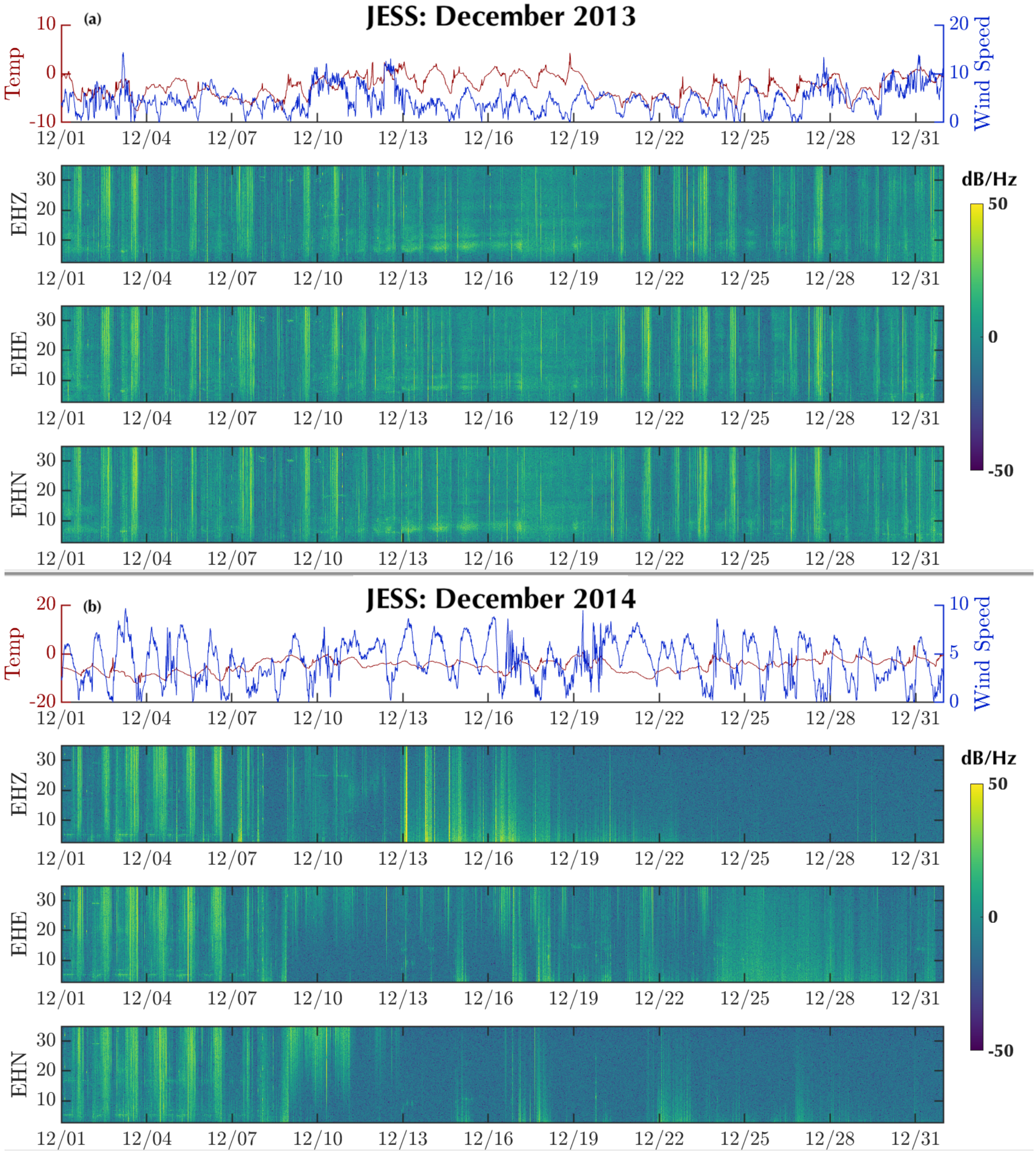

Figure S5. Spectrograms for station JESS for (a) December 2013 and (b) December 2014. During the second week of December 2014, data quality rapidly declines and never improves. Note different scales for temperature and wind speed for the two subplots.

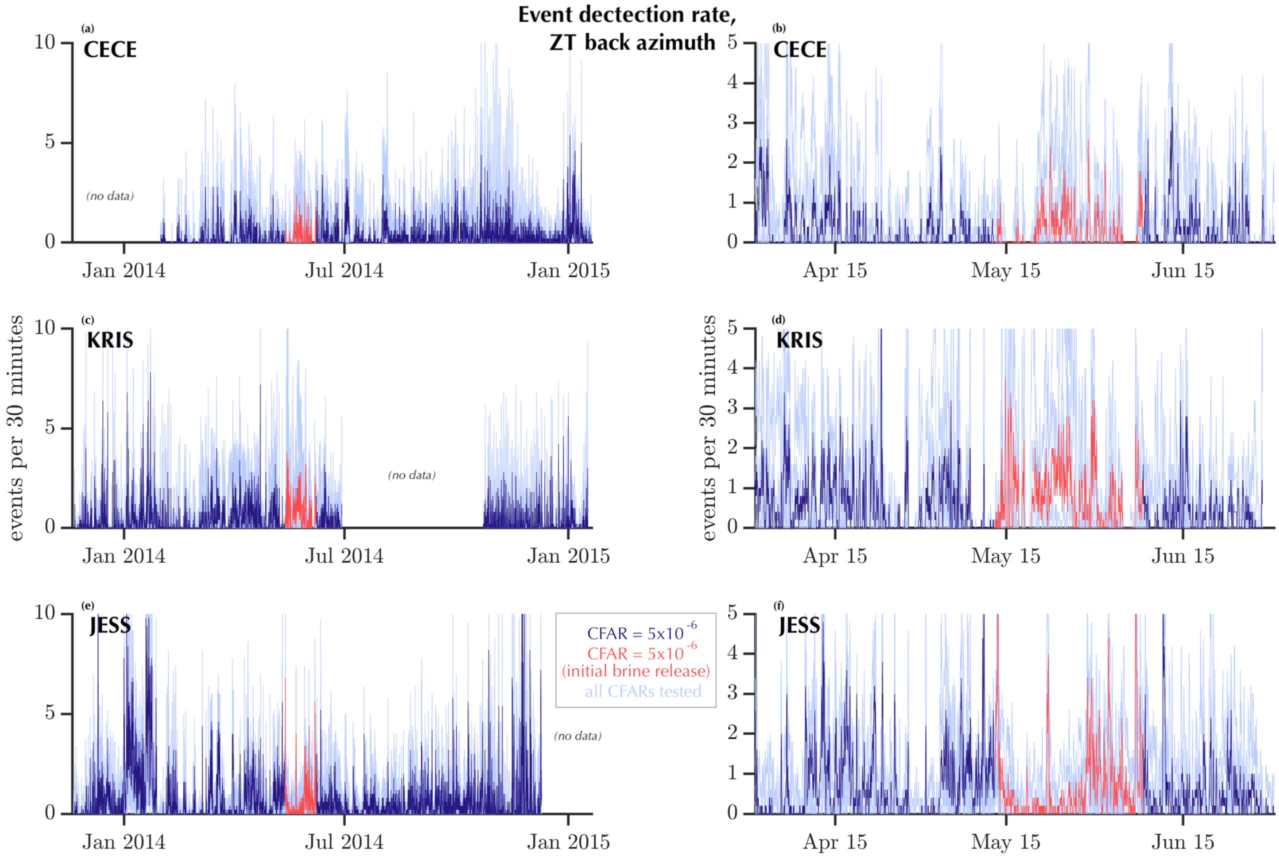

Figure S6. Events per 30 minutes detected by the Rayleigh-wave detector with the CFAR $= 5\text{x}10^{-6}$ condition highlighted, for events from non-Blood Falls back azimuths. See Figure 2 for the ZT back azimuth directions for each station. (a,b) land-based station CECE, (c,d) land-based station KRIS, and (e,f) on-ice station JESS (some rates above 10 events/30 minutes are cut off by the vertical scale). The left column is the entire data record from 20 November 2013 – 20 January 2015; the right column is from 1 April – 1 July 2014. On all panels, the initial brine release period 13 May – 8 June 2014 is highlighted in red. Light blue lines: events detected under all prescribed CFAR conditions, dark blue: events detected at the CFAR $= 5\text{x}10^{-6}$ level. All time series are smoothed with a 5-point (2-hour duration) moving window.

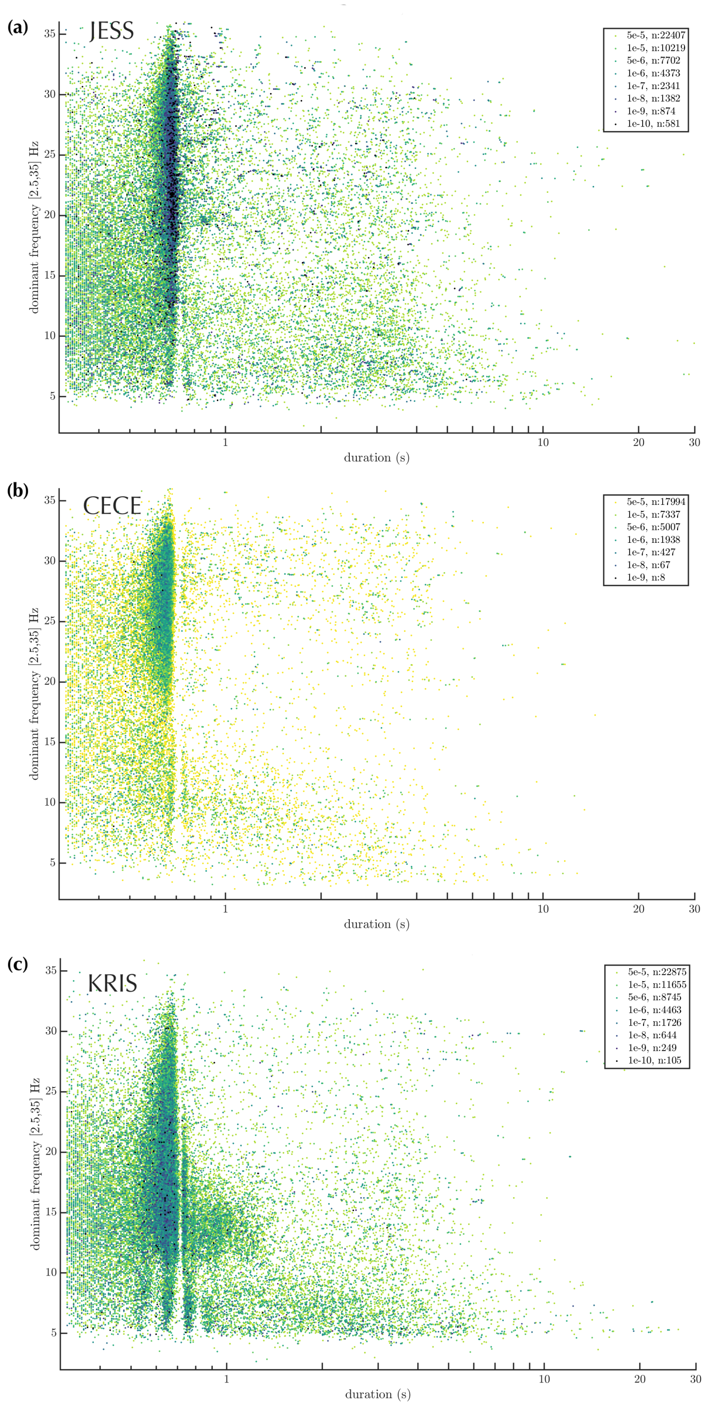

Figure S7. Dominant frequency on the vertical channel and event duration (log scale) for Rayleigh events identified with a Blood Falls back azimuth from each station. Darker colors indicate smaller CFAR values (higher threshold values). The legend for each plot lists the number of events identified under each CFAR condition, summed over the entire data period.

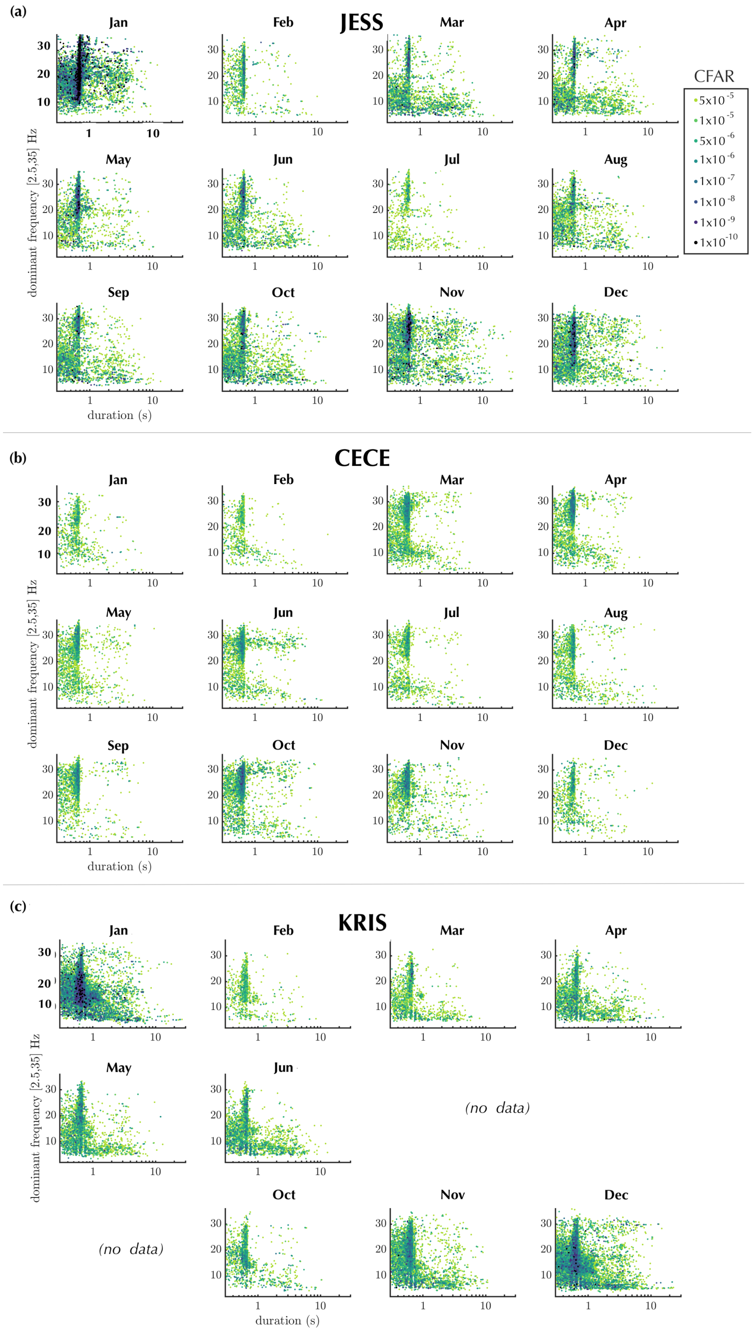

Figure S8. Dominant frequency on the vertical channel during Rayleigh events and event duration for Blood Falls back azimuth events for each station. Event duration is plotted on a log scale. Darker data points represent smaller CFAR values (larger threshold values). Plots for some station/month pairs include data from multiple years.

Figure S9. Various cracks in ice near the glacier terminus. Cracks include crevasses on the glacier near the cliff face, cracks in the ice-cored terminal moraine (sediment at left of photo), and in the lake ice where the person is standing. Photo: Chris Carr, photo date: November 2013.

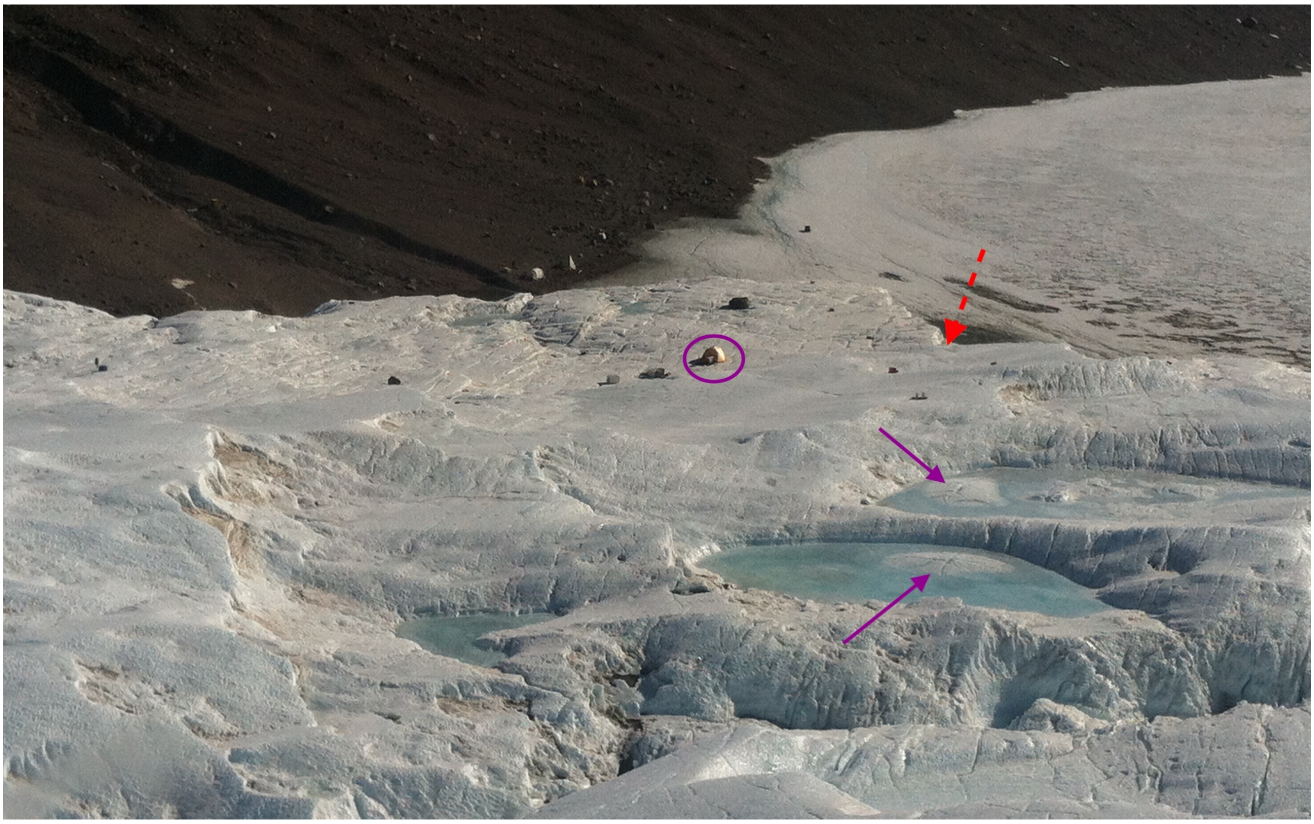

Figure S10. Ice blisters near Blood Falls. Two purple arrows mark ice blisters. The red dashed arrow points to the Blood Falls area of the terminus (out of view). For scale, a tent is circled in purple, this tent is in approximately the same location as the circled people in Figure S1. Photo: Chris Carr, photo date: 11 December 2013.

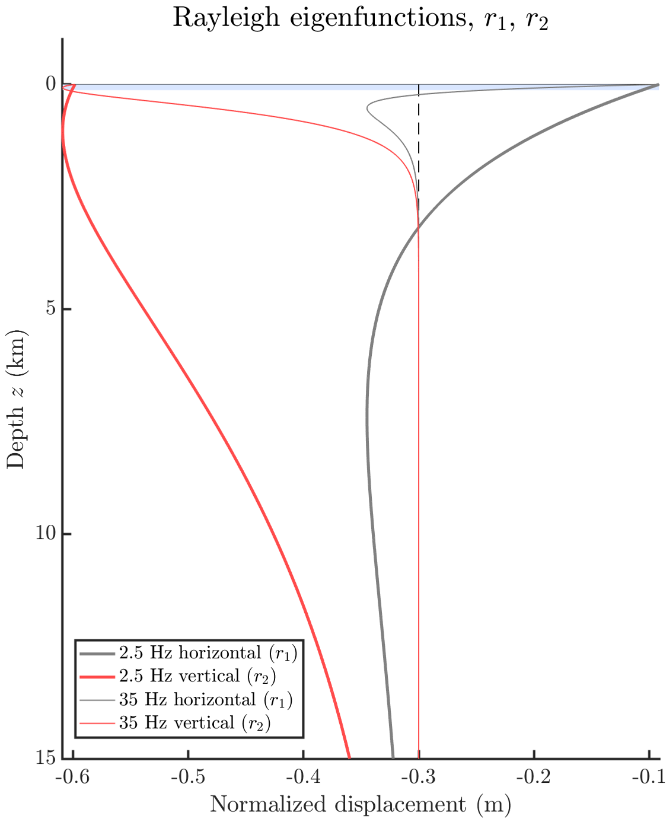

184

185 **Figure S11.** Frequency-dependent, normalized vertical and horizontal displacement as a
186 function of depth, calculated for the eigenfunctions described in the text. The light blue layer
187 represents the 50 m-thick glacier in our model.

Table S1. Rayleigh detector threshold values and sample variance for 20–22 May 2014 under the 5×10^{-6} CFAR condition, Blood Falls back azimuth. Threshold and sample variance were calculated for 30-minute windows. By definition, each 30-minute window has a single threshold value. We estimate the 30-minute window sample variance as the median of the individual sample variances for all samples within a 30-minute window, see table footnotes.

Station	Min ρ	Mean* ρ	Max ρ	Min $\hat{\sigma}^2$	Mean** $\hat{\sigma}^2$	Max $\hat{\sigma}^2$
CECE	0.6819	0.7657	0.9559	8.210	12.80	29.61
JESS	0.5774	0.8812	0.9961	10.98	163.4	1863
KRIS	0.7124	0.7868	0.9693	6.857	10.31	36.35

* $\frac{1}{m}\sum_1^m \rho_m$; where m indicates number of 30-minute windows.
** $\frac{1}{m}\sum_1^m [\text{median}(\hat{S}^2)]_m$; m as above.